

# $^{229}\text{Th}$ Nuclear Spectroscopy in an Opaque Material: Laser-Based Conversion Electron Mössbauer Spectroscopy of $^{229}\text{ThO}_2$

Ricky Elwell<sup>a,1</sup>, James E. S. Terhune<sup>a,1</sup>, Christian Schneider<sup>a,1</sup>, Harry W. T. Morgan,<sup>2</sup> Hoang Bao Tran Tan,<sup>3,4</sup> Udedhika C. Perera,<sup>3</sup> Daniel A. Rehn,<sup>4</sup> Marisa C. Alfonso,<sup>5</sup> Lars von der Wense,<sup>6</sup> Benedict Seiferle,<sup>7</sup> Kevin Scharl,<sup>7</sup> Peter G. Thirolf,<sup>7</sup> Andrei Derevianko,<sup>3</sup> and Eric R. Hudson<sup>1,8,9</sup>

<sup>1</sup>Department of Physics and Astronomy, University of California, Los Angeles, CA 90095, USA

<sup>2</sup>Department of Chemistry, University of Manchester, Oxford Road, Manchester M13 9PL, UK

<sup>3</sup>Department of Physics, University of Nevada, Reno, Nevada 89557, USA

<sup>4</sup>Computational Physics Division, Los Alamos National Laboratory,

P.O. Box 1663, Los Alamos, New Mexico 87545, USA

<sup>5</sup>Eckert & Ziegler Analytics, Inc., Atlanta, Georgia 30318, USA

<sup>6</sup>Department of Physics, Johannes Gutenberg-Universität Mainz, Mainz 55128, Germany

<sup>7</sup>Faculty of Physics, Ludwig-Maximilians-Universität München, 85748 Garching, Germany

<sup>8</sup>Challenge Institute for Quantum Computation, University of California Los Angeles, Los Angeles, CA, USA

<sup>9</sup>Center for Quantum Science and Engineering, University of California Los Angeles, Los Angeles, CA, USA

(Dated: September 16, 2025)

The exceptionally low-energy  $^{229}\text{Th}$  nuclear isomeric state is expected to provide a number of novel and powerful applications [1, 2], including the construction of a robust and portable solid-state nuclear clock [3], perhaps contributing to a redefinition of the second [4], exploration of nuclear superradiance [5, 6], and tests of fundamental physics [7–10]. Further, analogous to the capabilities of traditional Mössbauer spectroscopy, the sensitivity of the nucleus to its environment can be leveraged to realize *laser* Mössbauer spectroscopy and with it new types of strain and temperature sensors [3, 11] and a new probe of the solid-state environment [12], all with exquisite sensitivity. However, current paradigms for probing the nuclear transition in a solid require the use of a high band gap, vacuum-ultraviolet transmissive host, severely limiting the applicability of these techniques – e.g. so far laser excitation has only been demonstrated in the high band gap metal fluoride systems  $\text{CaF}_2$  [13],  $\text{LiSrAlF}_6$  [14], and  $\text{ThF}_4$  [15]. Here, we report the first demonstration of laser-induced conversion electron Mössbauer spectroscopy, which provides the ability to probe the nuclear transition in a material that is opaque to light resonant with the nuclear transition. Specifically, we excite the nuclear transition in a thin  $\text{ThO}_2$  sample whose band gap ( $\sim 6$  eV) is considerably smaller than the nuclear isomeric state energy (8.4 eV). As a result, the excited nucleus can quickly decay by internal conversion [16], resulting in the ejection of electrons from the surface. By collecting these conversion electrons, nuclear spectroscopy can be recorded. Unlike fluorescence spectroscopy, this technique is compatible with materials whose work function is less than the nuclear transition energy, opening a wider class of systems to study. Further, because  $\text{ThO}_2$  can be made from spinless isotopes [4] and the internal conversion decay process reduces the isomeric state lifetime to only  $\sim 10 \mu\text{s}$ , allowing  $\sim 10^8$  relative reduction in clock interrogation time, a conversion-electron-based nuclear clock could lead to a  $\sim 10^4$  improvement in clock instability.

The recent observation [13, 14] of direct laser excitation of the  $^{229}\text{Th}$  isomeric state in high band gap crystals has, after almost 50 years of work, opened the door to a laser-accessible nuclear transition and driven rapid progress in the development of solid-state optical clocks. Already, the nuclear transition frequency has been compared to an atomic clock and its linewidth studied [17], and work has begun to optimize the clock performance by developing both a theoretical understanding of nuclear quenching mechanisms [12] and using them to shorten the clock interrogation cycle [18, 19]. Similarly, excitation of the nuclear transition in a vacuum ultraviolet (VUV) transmissive thin film has opened the door to integrated-photonic-based nuclear clocks and sensors [15]. Further, new high bandgap materials have been analyzed that could provide dramatic simplification of the clock by, e.g., doping  $^{229}\text{Th}$  into a nonlinear optical crystal [20] and, by using principles of molecular design, provide a system with the potential for performance orders of magnitude beyond any current or planned optical clock [4, 21].

Because the  $^{229}\text{Th}$  nucleus provides a highly-controllable system which can be deployed into various hosts, it is expected, in analogy to Mössbauer spectroscopy, that these same techniques can also be used as new probes of the

<sup>a</sup> These authors contributed equally to the work.

solid-state chemical and nuclear environment. However, in all studies to date, nuclear excitation is detected by observing the resulting nuclear fluorescence, which requires the material band gap to be larger than the isomeric transition energy ( $> E_{\text{iso}}$ ). This requirement severely limits the material hosts available for study and, therefore, it is highly desirable to extend the spectroscopy of the isomeric transition to low band gap ( $< E_{\text{iso}}$ ) environments.

Conversion electron Mössbauer spectroscopy (CEMS) of  $^{229}\text{Th}$  has been proposed as a method to extend the technique of laser-based nuclear spectroscopy to low band gap materials [22, 23]. CEMS utilizes the fact that if the nuclear energy is larger than the material band gap, the internal conversion (IC) relaxation process is possible by promoting an electron across the band gap [16, 24]. If this promoted IC electron originates in a shallow-enough state in the valence band, the electron can overcome the work function barrier and emerge from the material surface. By detecting these conversion electrons, nuclear spectroscopy can be recorded.

In addition to providing a means to study low band gap materials, CEMS could also allow significant improvements in nuclear clock stability as the IC decay rate is roughly  $10^8$  times faster than the radiative decay rate, enabling a much faster clock interrogation rate, leading to a projected clock instability of  $\sim 10^{-18}$  at 1 s. Further, a CEMS-based nuclear clock could operate by simply reading out the CEMS photocurrent, providing a means to greatly simplify and miniaturize future nuclear clocks [25].

Here, we report the first demonstration of laser-based CEMS of any nucleus. Specifically, a VUV laser system is used to excite  $^{229}\text{Th}$  nuclei in a thin sample of thoria ( $\text{ThO}_2$ ).  $^{229}\text{ThO}_2$  was chosen as the first host as it has a low band gap ( $\sim 6$  eV [26]) and is readily available as a stoichiometric Th compound. Conversion electrons from the  $^{229}\text{ThO}_2$  are detected as a function of laser excitation energy providing the first laser-based CEMS nuclear spectrum, which determines the  $^{229}\text{Th}$  nuclear transition frequency as  $2020407.5(2)_{\text{stat}}(30)_{\text{sys}}$  GHz, consistent with previously reported values of the transition [13–15, 17], and whose width is consistent with the laser linewidth of our system reported in previous studies [14, 15]. Further, the IC lifetime is measured as  $\sim 10 \mu\text{s}$ , which is consistent with that measured in  $^{229}\text{Th}$  implantation studies [27] and theoretical calculations of the IC lifetime described below.

In what follows we describe the  $^{229}\text{ThO}_2$  target, experimental apparatus, and the spectroscopic protocol, before presenting the results of the CEMS spectroscopy. Next, we present calculations of the isomer shift and IC lifetime in  $^{229}\text{ThO}_2$  using a theoretical approach that combines solid-state density functional theory and relativistic atomic many-body perturbation theory methods. Following these results, we use the measured lifetime of the internal conversion decay of the isomeric state in  $^{229}\text{ThO}_2$  to evaluate the ideal performance of a  $^{229}\text{ThO}_2$  conversion electron clock, and find its projected instability to be  $\sim 2 \times 10^{-18}$  at 1 s.

## $^{229}\text{ThO}_2$ Target and Apparatus

The CEMS target was constructed by electrodepositing  $^{229}\text{ThO}_2$  onto a stainless steel disk (see Fig. 1 for image of target, procured from Eckert & Ziegler Analytics, Inc.). Although other oxide and hydroxide compounds of Th may be present in the target, this paper assumes that the predominant chemical form of  $^{229}\text{Th}$  in the target is  $^{229}\text{ThO}_2$ , based on the method of target preparation (see SI for details). The diameter of the  $^{229}\text{ThO}_2$  is  $\approx 5$  mm and its thickness is estimated from the width of the  $\alpha$ -particle spectrum as  $\sim 10$  nm (Fig. 1(c)), which is consistent with a measured total activity of  $\approx 6.3$  kBq. The VUV absorption of  $\text{ThO}_2$  is estimated as  $\alpha \approx 0.1 \text{ nm}^{-1}$  [28], implying that  $^{229}\text{Th}$  nuclei within a depth of  $\approx 10$  nm can be efficiently excited by the laser. In addition, the inelastic mean free path of electrons in solids at the eV energy scale is typically  $\sim 10$  nm [29], meaning that an IC electron generated at greater depths likely scatters before extraction from the surface. As such, further  $^{229}\text{ThO}_2$  thickness primarily contributes to the background in the form of electrons produced via radioactive decays [30], and thus a thickness of  $\approx 10$  nm is likely optimal for CEMS.

CEMS spectroscopy is recorded by directing a tunable VUV laser onto the  $^{229}\text{ThO}_2$  target. Briefly, VUV radiation was produced via resonance-enhanced four-wave mixing of two pulsed dye lasers in Xe gas. The frequency of the first pulsed dye laser,  $\omega_u$ , was locked to the  $5p^6 \ ^1S_0 \rightarrow 5p^5 \left( ^2P_{3/2}^o \right) 6p \ ^2[1/2]_0$  two-photon transition of Xe at  $\sim 249.63$  nm. The frequency of the second pulsed dye laser,  $\omega_v$ , was scanned to produce VUV radiation in the Xe cell given by the difference mixing relation  $\omega = 2\omega_u - \omega_v$ . All three laser beams then impinge off-axis with respect to a  $\text{MgF}_2$  lens, whose chromatic dispersion is used with downstream pinholes to spatially filter the VUV beam and pass it towards the  $^{229}\text{ThO}_2$  spectroscopy chamber. The laser system delivers 30 pulses per second to the target with a typical VUV pulse energy of  $\sim 6 - 8 \mu\text{J}/\text{pulse}$  (see Refs. [14, 32] for details). For these experiments,  $\text{N}_2$  gas is added to the Xe cell to quench a process leading to amplified spontaneous emission at 147 nm (see SI for details), which occurs on a timescale similar to IC decay and otherwise contributes to the photoelectron background.

The  $^{229}\text{ThO}_2$  target is held in a custom mount (see Fig. 1(a)) that provides the ability to electrically bias the

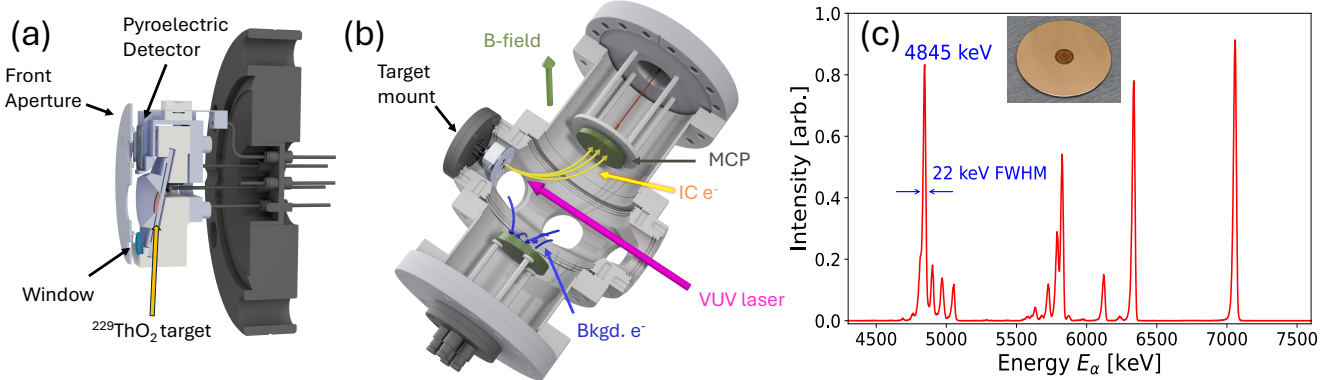


FIG. 1. (a) Cut-away rendering of the  $^{229}\text{ThO}_2$  target mount. Arrows denote front aperture, window, target, and pyroelectric detector. (b) Rendering of the spectroscopy chamber. (Magenta arrow) Direction of VUV laser propagation. (Yellow arrows) IC electron trajectories from target to detection MCP. (Blue arrows) Background photoelectrons generated from VUV scatter diverted to secondary electrode. (Green arrow) Direction of static B-field used to guide IC electrons. (c)  $\alpha$ -spectrum of the  $^{229}\text{ThO}_2$  target. (Inset) Photograph of  $^{229}\text{ThO}_2$  target used in this study. The peak labeled to 4845 keV corresponds to the dominant  $\alpha$ -decay mode of  $^{229}\text{Th}$ . The other large peaks correspond to the  $\alpha$ -decays of daughter nuclei. The  $^{229}\text{Th}$  peak had a FWHM of  $\sim 22$  keV, consistent with energy loss through a  $\sim 10$  nm sample, as estimated with SRIM [31].

sample, as well as VUV laser monitoring capabilities. Biasing of the target is necessary as the VUV laser causes a prompt burst of photoelectrons when it impinges on the  $^{229}\text{ThO}_2$  target, which will overwhelm the electron detector. These initial photoelectrons are suppressed for the first  $\sim 100$  ns after the laser pulse by positively biasing the  $^{229}\text{ThO}_2$  target to 135 V, before the bias voltage is changed to -405 V to aid the extraction of IC electrons from the surface; at all times the front aperture of the mount is held at 100 V. The mount also houses a fused silica target that fluoresces under VUV illumination aiding alignment and a bare pyroelectric crystal to provide *in situ* monitoring of the VUV laser pulse energy. The target chamber is mounted on a combined lever arm-stepper motor system that allows it to be raised and lowered, causing the VUV laser to illuminate either the  $^{229}\text{ThO}_2$  target or laser energy monitor. To limit hydrocarbon buildup on the target and to limit scattering of the IC electrons due to background gases, the target chamber was ozone plasma cleaned prior to baking, and operated at a pressure of  $\sim 10^{-7}$  Pa.

In principle, IC electron detection can be accomplished by simply positively biasing, e.g., a multi-channel plate (MCP) detector held near the  $^{229}\text{ThO}_2$ . However, it was found that scattered light from the VUV laser generated a large afterglow of photoelectrons originating at positions dispersed throughout the chamber which lasted tens of microseconds – presumably due to fluorescence of components within the beamline and chamber. To overcome this background, a combination of electric and magnetic fields were used that focused electrons originating from the  $^{229}\text{ThO}_2$  target onto a detection MCP, while diverting electrons generated elsewhere to another region of the chamber (see SI). Finally, as an additional layer of protection for the detection MCP, its front plate voltage was controlled so that it had no gain during the initial burst of photoelectrons from the target.

### Spectroscopy

Using this apparatus, CEMS was performed by recording the number of detected electrons in the window between 6  $\mu\text{s}$  and 40  $\mu\text{s}$  after each laser pulse as a function of VUV laser wavelength; this window was chosen based on previous theoretical estimates [24] and observations of IC decay [33] following  $^{233}\text{U}$  decay. The electron signal, normalized by the laser pulse energy, is shown in Fig. 2(a) as a function of frequency for a region  $\sim 100$  GHz wide and centered on the  $^{229}\text{Th}$  nuclear transition energy. These data were recorded by firstly measuring the pulse energy, then detecting the total number of electrons emitted after 36,000 pulses (20 minutes) before measuring the pulse energy again. This process was repeated to record a laser CEMS spectrum. The data in Fig. 2(a) is the average of four spectra with the vertical error bars representing the standard error. Due to differences in system alignment between campaigns, the photoelectron background varied slightly between different spectra. Therefore, a Lorentzian with a background fit was used to determine and subtract the photoelectron background before the data is combined. Further, because the laser frequency is not perfectly controlled these spectra are binned in frequency and the horizontal error bars are the standard deviation of the frequency. Each data point represents the average of at least 140,000 laser pulses.

A nonlinear, least squares fit of a Lorentzian to the spectrum yields a central value of  $2020407.5(2)_{\text{stat}}(30)_{\text{sys}}$  GHz

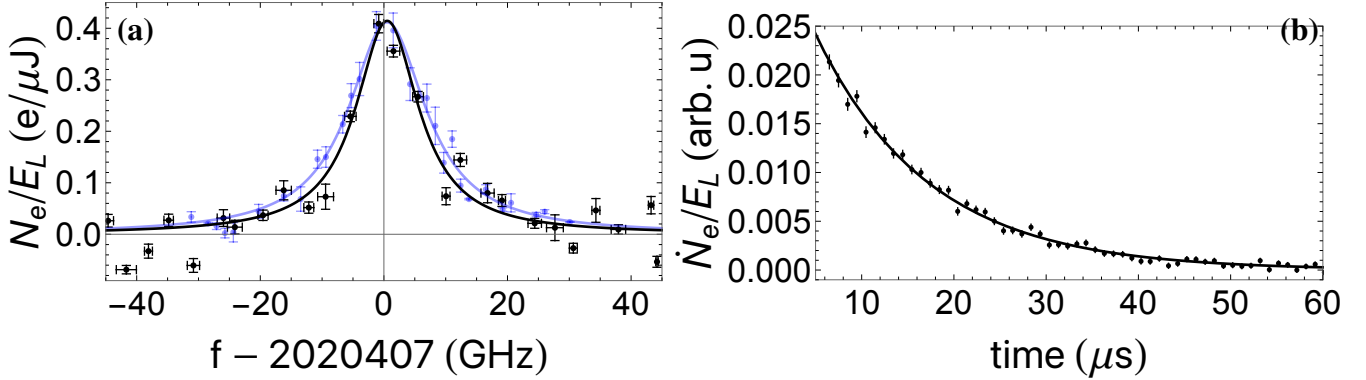


FIG. 2. (a) The laser-based CEMS spectra of  $^{229}\text{ThO}_2$  is shown in black with a fit of a Lorentzian profile. Each point is an average of  $\geq 140,000$  laser pulses. A constant baseline of  $\approx 75 \text{ e}^-$  per laser pulse has been subtracted. The vertical error bars denote the standard error, while the horizontal error bars are the standard deviation of the laser frequency for the points in the bin. For comparison, the radiative decay spectrum of  $^{229}\text{Th:LiSrAlF}_6$ , taken from Ref. [14], is shown in blue. (b) The IC decay rate as a function of time is shown in black alongside a fit of a decaying exponential with a background, leading to an IC lifetime of  $12.3(3) \mu\text{s}$ .

and full-width-half-maximum linewidth of  $12.4(4) \text{ GHz}$ , both consistent with our observations in  $\text{LiSrAlF}_6$  [14] and  $\text{ThF}_4$  [15]. Here, statistical error is the 68% confidence interval and the systematic uncertainty is predominantly due to the accuracy of the wavemeter and likely conservative. On resonance, an average of  $0.41(5) \text{ e}/\mu\text{J}$  per laser pulse is detected. The expected signal can be estimated as  $\eta_e \eta_c N_e \times e^{-t_i/\tau_{\text{IC}}}$ , where  $\eta_e$  is the extraction of efficiency of IC electrons from the sample,  $\eta_c$  is the collection efficiency of electrons emitted from the sample,  $N_e$  is the number of excited  $^{229}\text{Th}$  nuclei, and  $t_i$  is the time that electron counting begins after the laser pulse. Based on calibrations of the apparatus (see SI), the expected signal is found as  $0.15^{+0.25}_{-0.09} \text{ e}^-/\mu\text{J}$ , in reasonable agreement with the recorded spectrum.

Using the same system, the lifetime of the IC decay is measured by comparing the time binned electron counts collected on resonance in the first  $190 \mu\text{s}$  after laser excitation. Specifically, the average number of time binned electron counts per  $\mu\text{J}$  of laser energy is obtained for both the on and off ( $\sim 100 \text{ GHz}$  detuning) resonant illumination periods. The average off resonance counts are then subtracted from the average on resonance counts to remove any photoelectron background, and the result is plotted in Fig. 2(b). A background free nonlinear least-squares fit of a decaying exponential reveals an IC lifetime of  $12.3(3) \mu\text{s}$ , as shown in Fig. 2(b). As discussed later, the IC decay rate is sensitive to the local chemical environment, so a range of decay rates is possible and this lifetime should be interpreted as an estimate.

### Calculation of Isomer Shifts and Internal Conversion Lifetime in $^{229}\text{ThO}_2$

The measured isomer energy is in agreement with the earlier spectroscopic experiments in three wide band gap hosts [13–15]. Theoretically, this is supported by the calculations [34] of isomer shifts for a large variety of  $^{229}\text{Th}$  solid-state hosts and by our  $^{229}\text{ThO}_2$ -specific calculations presented in the SI. For example, we expect that the isomer shift between bulk  $^{229}\text{ThO}_2$  and  $^{229}\text{Th:LiSrAlF}_6$  is on the order of 100 MHz, well below the  $\sim 3 \text{ GHz}$  reported experimental resolution. Our calculations predict the nuclear transition frequency for bulk  $^{229}\text{ThO}_2$  to be  $2,020,407,338(70) \text{ MHz}$ .

In the IC process, the energy of the excited nucleus is transferred to the electrons. In a crystalline solid, that means promoting a valence band electron  $|v\mathbf{k}\sigma_v\rangle$  into a conduction band state  $|c\mathbf{k}\sigma_c\rangle$  and creating a hole in the valence band (Fig. 3(a)). The process is mediated by the hyperfine interaction (HFI)  $W$  which, for periodic lattices, conserves the electronic crystal momentum  $\mathbf{k}$ , but can connect electronic states of different spin projections  $\sigma_{v,c}$ . We derived the rate for the described IC process (see SI) as

$$\Gamma_{\text{IC}} = \frac{2\pi}{\hbar} \frac{1}{2I_e + 1} \sum_{M_g M_e} \sum_{\sigma_c \sigma_v} \overline{|W_{c\sigma_c v\sigma_v}^{ge}(\mathbf{k})|^2} G_{cv}(\hbar\omega_{\text{nuc}}). \quad (1)$$

Here  $|e\rangle$  and  $|g\rangle$  are the isomer and the ground nuclear states with spins  $I_{e,g}$  and magnetic quantum numbers  $M_{e,g}$ . The HFI  $W$  connects the two nuclear states and the valence and conduction band electronic states.  $G_{cv}(\hbar\omega_{\text{nuc}})$  is the

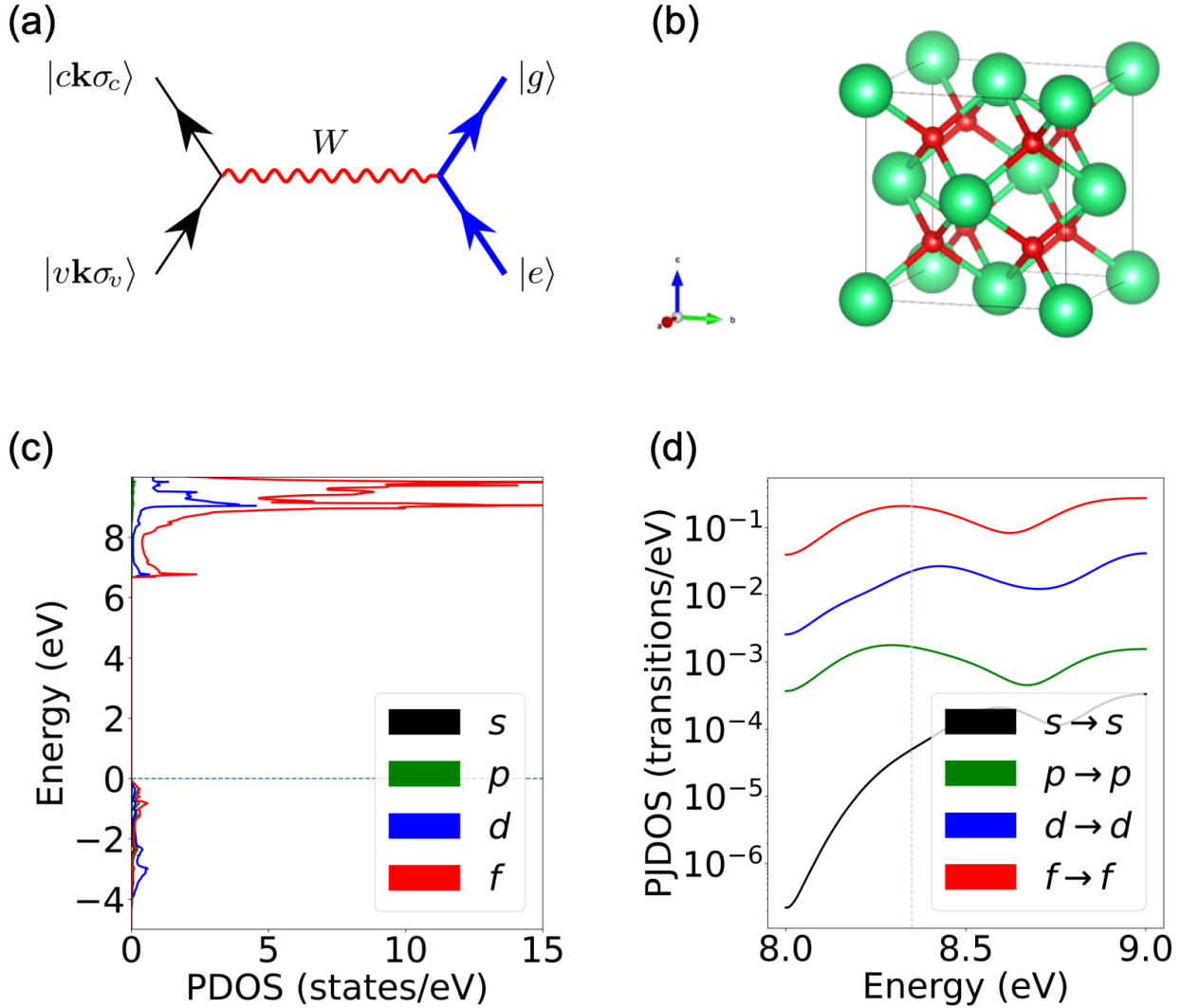


FIG. 3. (a) Feynman diagram of the internal conversion process. The interaction is mediated by a virtual photon exchange, corresponding to the hyperfine interaction  $W$ . The crystal momentum  $\mathbf{k}$  is conserved in this process. (b) Conventional unit cell of  $\text{ThO}_2$  with Th atoms in green and O atoms in red. (c) Th projected density of states (PDOS) computed with  $G_0W_0$ . The horizontal dashed line denote the Fermi level. (d) Th projected joint density of states (PJ DOS) computed with  $G_0W_0$ . The vertical dashed line denotes the nuclear isomeric energy.

conventional [35] Joint Density of States (JDOS) at the nuclear transition energy  $\hbar\omega_{\text{nuc}}$ . The bar denotes averaging over a surface of constant energy in  $\mathbf{k}$ -space.

The same JDOS appears in the theory of electromagnetic interband absorption [35] and is clearly a highly material-dependent quantity. Therefore, to understand the physics of the IC process, and in particular its rate, we calculated the properties of  $^{229}\text{ThO}_2$  with periodic electronic structure theory ( $GW$  and DFT). The calculations used the  $G_0W_0$  approximation for the electronic self-energy and the Bethe–Salpeter Equation (BSE) for optical properties (see SI for details). The fundamental band gap computed with  $G_0W_0$  is 6.2 eV, in good agreement with experimental values [36, 37] (calculation details provided in the SI).

The absorption spectrum, computed with  $G_0W_0$ +BSE, agrees with the measurements in Ref. [28], supporting our estimation of  $\alpha \approx 0.1 \text{ nm}^{-1}$ .

$\text{ThO}_2$  crystallizes in the fluorite structure (space group  $Fm\bar{3}m$ , #225), where each Th atom is coordinated by eight oxygen atoms in a cubic arrangement (Fig. 3(b)). The  $\text{Th}^{4+}-\text{O}^{2-}$  bonding is predominantly ionic with a modest

covalent admixture arising from overlap of Th  $6d/5f$  and O  $2p$  orbitals. That Th is in the +4 oxidation state may be verified from the projected density of states (PDOS) on Th, where the  $5f$  and  $6d$  components in the valence band are nearly empty. In contrast, the Th  $5f$  and  $6d$  valence orbitals form large peaks in the conduction band, indicating the transfer of an electron from an  $O^{2-}$  anion to form  $Th^{3+}$ . Both the valence and conduction bands contain small contributions from Th-projected  $p$  orbitals. As it turns out, the IC process primarily involves transferring electrons between these  $p$ -orbital components.

In computing the HFI matrix element in Eq. (1), it is convenient to project the valence and conduction band states  $|v\mathbf{k}\sigma_v\rangle$  and  $|c\mathbf{k}\sigma_c\rangle$  onto the basis of Th atomic orbitals. The matrix element  $W_{c\sigma_c v\sigma_v}^{ge}(\mathbf{k})$  may then be expressed as a sum over different HFI matrix elements connecting atomic orbitals of definite angular momenta, weighted by the expansion coefficients of  $|v\mathbf{k}\sigma_v\rangle$  and  $|c\mathbf{k}\sigma_c\rangle$ . To the lowest order, cross terms arising when squaring the expansion of  $W_{c\sigma_c v\sigma_v}^{ge}(\mathbf{k})$  can be neglected. This allows the expression of the IC rate in terms of the nuclear ground state HFI constants  $A$  and the “projected joint density of states” (PJ DOS) in Th. The PJ DOS is a JDOS weighted by the projections of the crystal electronic states onto the thorium atomic orbitals that allows us to describe the character of the delocalized crystal orbitals close to the thorium nucleus (see SI). The HFI  $A$  constants for  $Th^{3+}$  are known from experiments and high-precision relativistic atomic-structure calculations, see Ref. [12]. The PJ DOS of transitions with the largest contributions to the IC rate are shown in Fig. 3(c).

Using these values, we arrive at an estimate for the IC rate of  $\Gamma_{IC} \approx 1.3 \times 10^4 \text{ s}^{-1}$ , corresponding to an IC lifetime of  $\approx 80 \mu\text{s}$ .

Sources of the disparity between the measured and theoretical lifetimes could include known errors in the local projections of the plane wave orbitals done by VASP [38], small changes to the valence and conduction states expected with the addition of spin-orbit coupling in solid-state calculations, cross- and higher-order expansion terms neglected in our evaluation of the rate (1), and deviations of the sample from bulk  $^{229}\text{ThO}_2$  due to both surface and self-radiation damage effects. Compared to the pristine  $^{229}\text{ThO}_2$ , the IC rate for  $^{229}\text{Th}$  adjacent to point defects can be enhanced by the electric quadrupole HFI contribution [39] due to symmetry breaking. Nevertheless, the order of magnitude agreement supports the physical interpretation that observed IC decay results from the nucleus relaxing via transferring an electron from an oxide anion into the Th  $6p$  component of the conduction band.

### Projected Clock Performance

In addition to its use as a new chemical probe, laser-based CEMS may allow the construction of a new type of nuclear clock with several advantages over crystal-based clocks [40]. Chief among these advantages are a greatly reduced clock interrogation time, as the IC decay rate is about  $10^8$  times faster than radiative decay, and the potential for clock readout by simply monitoring the current leaving the target, which could facilitate dramatic miniaturization.

For such a clock, assuming  $^{229}\text{ThO}_2$  is produced from  $^{16}\text{O}$ , the largest sources of instability would be broadening due to magnetic dipole interactions between the  $^{229}\text{Th}$  nuclei and lifetime broadening. Given that the Th-Th distance in  $\text{ThO}_2$  is  $3.96 \text{ \AA}$  [41], the expected Zeeman broadening due to neighboring  $^{229}\text{Th}$  nuclei is  $\sim 10 \text{ Hz}$ . Thus, the primary source of instability is the lifetime broadening of  $\Gamma \approx 2\pi \times 16 \text{ kHz}$ . Assuming a polished face of a  $\sim 10 \text{ nm}$  thick single crystal is prepared and realizes an electron extraction efficiency  $\eta_e \approx 0.5$  [29], and that the photoelectron background is eliminated by material purification and baffling, a  $100 \mu\text{W}$  laser leads to a projected clock instability of  $\sim 2 \times 10^{-18}$  at 1 s averaging. Interestingly, it is possible that the electric current from the IC process could also be used as a form of readout, as it would generate a current of  $\sim 300 \text{ nA}$  on the  $\mu\text{s}$  timescale, providing a simple means for clock operation and locking [25].

### DISCUSSION AND OUTLOOK

With this first demonstration of laser-based CEMS, an entirely new class of materials is now compatible with laser nuclear spectroscopy. By implanting  $^{229}\text{Th}$  into low band gap materials and observing both the lifetime of the internal conversion decay channel and the isomer shift of the transition, detailed information can be gathered about the local phononic, electronic, and nuclear structure. This in turn allows the isomeric transition to serve as a sensor of strain and temperature in the solid [11, 42]. Further, at the energy scale of the IC electrons, their inelastic mean free path is a sensitive function of their energy relative to the Fermi level [29]. In the future, it may be possible to relate the efficiency with which IC electrons emerge from a surface with both the surface quality and the band structure local to the implanted  $^{229}\text{Th}$ . Looking further forward, off-resonant excitation of  $^{229}\text{Th}$  nuclei through a combined nuclear and phononic transition in the solid could enable laser-based nuclear resonance vibrational spectroscopy [43, 44]. This

could enable measurement of the local phonon density of states with sub- $\mu$ eV precision, considerably beyond what is possible with conventional Mössbauer spectroscopy [44].

Given our previous work in  $^{229}\text{ThF}_4$  films [15], it can be concluded that as the  $^{229}\text{Th}$  is converted from the oxide to the fluoride state, the  $^{229}\text{Th}$  isomer will convert from decaying by IC to decaying by the emission of a VUV photon. Thus, the relative ratio of radiative decay to conversion electron decay following laser excitation could provide a new battery of methods to characterize the chemical state of Th compounds, perhaps aiding studies of nuclear power generation [45].

Additionally, laser-based CEMS provides a new platform to realize a solid-state Th clock that benefits from the inherent ease of a production of stoichiometric Th compounds, a  $10^8$  reduction in clock interrogation cycle, and the potential for a current-based readout allowing simplification and miniaturization of future nuclear clocks.

## ACKNOWLEDGEMENT

This work was supported by NSF awards PHYS-2013011, PHY-2412869 and PHY-2207546, and ARO award W911NF-11-1-0369. PGT and KS acknowledge support by BaCaTeC (Grant 7 [2029-2]). ERH acknowledges institutional support by the NSF QLCI Award OMA-2016245.

This work used Bridges-2 at Pittsburgh Supercomputing Center through allocation PHY230110 from the Advanced Cyberinfrastructure Coordination Ecosystem: Services & Support (ACCESS) program, which is supported by National Science Foundation grants #2138259, #2138286, #2138307, #2137603, and #2138296. DAR acknowledges support from the Institutional Computing Program at Los Alamos National Laboratory, via the Center for Integrated Nanotechnologies, a DOE BES user facility, for computational resources.

---

[1] E. V. Tkalya, V. O. Varlamov, V. V. Lomonosov, and S. A. Nikulin, Processes of the nuclear isomer  $^{229m}\text{Th}(3/2^+, 3.5 \pm 1.0 \text{ eV})$  resonant excitation by optical photons, *Phys. Scr.* **53**, 296 (1996).

[2] E. Peik and C. Tamm, Nuclear laser spectroscopy of the 3.5 ev transition in th-229, *Europhysics Letters* **61**, 181 (2003).

[3] W. G. Rellergert, D. DeMille, R. R. Greco, M. P. Hehlen, J. R. Torgerson, and E. R. Hudson, Constraining the evolution of the fundamental constants with a solid-state optical frequency reference based on the  $^{229}\text{Th}$  nucleus, *Phys. Rev. Lett.* **104**, 200802 (2010).

[4] H. W. T. Morgan, J. E. S. Terhune, R. Elwell, H. B. T. Tan, U. C. Perera, A. Derevianko, E. R. Hudson, and A. N. Alexandrova, A spinless crystal for a high-performance solid-state  $^{229}\text{Th}$  nuclear clock (2025), [arXiv:2408.12309](https://arxiv.org/abs/2408.12309).

[5] R. H. Dicke, Coherence in spontaneous radiation processes, *Phys. Rev.* **93**, 99 (1954).

[6] W.-T. Liao, S. Das, C. H. Keitel, and A. Pálffy, Coherence-Enhanced Optical Determination of the  $^{229}\text{Th}$  Isomeric Transition, *Phys. Rev. Lett.* **109**, 262502 (2012).

[7] V. V. Flambaum, Enhanced Effect of Temporal Variation of the Fine Structure Constant and the Strong Interaction in  $^{229}\text{Th}$ , *Physical Review Letters* **97**, 92502 (2006).

[8] V. V. Flambaum and R. B. Wiringa, Enhanced effect of quark mass variation in  $^{229}\text{Th}$  and limits from Oklo data, *Phys. Rev. C* **79**, 034302 (2009).

[9] E. Fuchs, F. Kirk, E. Madge, C. Paranjape, E. Peik, G. Perez, W. Ratzinger, and J. Tiedau, Searching for dark matter with the  $^{229}\text{Th}$  nuclear lineshape from laser spectroscopy, *Phys. Rev. X* **15**, 021055 (2025).

[10] D. Antypas et al., New horizons: Scalar and vector ultralight dark matter, [arXiv:2203.14915v1](https://arxiv.org/abs/2203.14915v1) (2022).

[11] J. S. Higgins, T. Ooi, J. F. Doyle, C. Zhang, J. Ye, K. Beeks, T. Sikorsky, and T. Schumm, Temperature sensitivity of a thorium-229 solid-state nuclear clock, *Phys. Rev. Lett.* **134**, 113801 (2025).

[12] H. W. T. Morgan, H. B. Tran Tan, R. Elwell, A. N. Alexandrova, E. R. Hudson, and A. Derevianko, Theory of internal conversion of the  $^{229}\text{Th}$  nuclear isomer in solid-state hosts (2024), [arXiv:2411.15641](https://arxiv.org/abs/2411.15641).

[13] J. Tiedau, M. V. Okhapkin, K. Zhang, J. Thielking, G. Zitzer, E. Peik, F. Schaden, T. Pronebner, I. Morawetz, L. Toscani De Col, et al., Laser excitation of the Th-229 nucleus, *Phys. Rev. Lett.* **132**, 182501 (2024).

[14] R. Elwell, C. Schneider, J. Jeet, J. Terhune, H. Morgan, A. Alexandrova, H. Tran Tan, A. Derevianko, and E. R. Hudson, Laser excitation of the  $^{229}\text{Th}$  nuclear isomeric transition in a solid-state host, (2024).

[15] C. Zhang, L. von der Wense, J. F. Doyle, J. S. Higgins, T. Ooi, H. U. Friebel, J. Ye, R. Elwell, J. E. S. Terhune, H. W. T. Morgan, A. N. Alexandrova, H. B. Tran Tan, A. Derevianko, and E. R. Hudson,  $^{229}\text{ThF}_4$  thin films for solid-state nuclear clocks, *Nature* **636**, 603 (2024).

[16] E. V. Tkalya, A. N. Zherikhin, and V. I. Zhudov, Decay of the low-energy nuclear isomer  $^{229}\text{Th}^m(3/2^+, 3.5 \pm 1.0\text{eV})$  in solids (dielectrics and metals): A new scheme of experimental research, *Phys. Rev. C* **61**, 064308 (2000).

[17] C. Zhang, T. Ooi, J. S. Higgins, J. F. Doyle, L. von der Wense, K. Beeks, A. Leitner, G. A. Kazakov, P. Li, P. G. Thirolf, T. Schumm, and J. Ye, Frequency ratio of the  $^{229m}\text{Th}$  nuclear isomeric transition and the  $^{87}\text{Sr}$  atomic clock, *Nature* **633**, 63 (2024), [arXiv:2406.18719](https://arxiv.org/abs/2406.18719).

[18] J. E. S. Terhune, R. Elwell, H. B. T. Tan, U. C. Perera, H. W. T. Morgan, A. N. Alexandrova, A. Derevianko, and E. R. Hudson, *Photo-Induced Quenching of the  $^{229}\text{Th}$  Isomer in a Solid-State Host* (2024), [arXiv:arXiv:2412.08998](https://arxiv.org/abs/2412.08998).

[19] F. Schaden, T. Riebner, I. Morawetz, L. T. De Col, G. A. Kazakov, K. Beeks, T. Sikorsky, T. Schumm, K. Zhang, V. Lal, G. Zitter, J. Tiedau, M. V. Okhaphin, and E. Peik, *Laser-Induced Quenching of the  $\text{Th-229}$  Nuclear Clock Isomer in Calcium Fluoride* (2024), [arXiv:2412.12339](https://arxiv.org/abs/2412.12339).

[20] H. W. T. Morgan, R. Elwell, J. E. S. Terhune, H. B. Tran Tan, U. C. Perera, A. Derevianko, A. N. Alexandrova, and E. R. Hudson, Proposal and theoretical investigation of  $^{229}\text{Th}$ -doped nonlinear optical crystals for compact solid-state clocks, *Appl. Phys. Lett.* **126**, 111101 (2025), [arXiv:2410.23364](https://arxiv.org/abs/2410.23364).

[21] H. W. T. Morgan, H. B. Tran Tan, A. Derevianko, R. Elwell, J. E. S. Terhune, E. R. Hudson, and A. N. Alexandrova, Design of new thorium nuclear clock materials based on polyatomic ions [10.26434/chemrxiv-2025-z2bkd](https://doi.org/10.26434/chemrxiv-2025-z2bkd) (2025).

[22] L. von der Wense et al., A laser excitation scheme for  $^{229}\text{Th}$ , *Phys. Rev. Lett.* **119**, 132503 (2017).

[23] L. C. von der Wense, B. Seiferle, C. Schneider, J. Jeet, I. Amersdorffer, N. Arlt, F. Zacherl, R. Haas, D. Renisch, P. Mosel, P. Mosel, M. Kovacev, U. Morgner, C. E. Düllmann, E. R. Hudson, and P. G. Thirolf, The concept of laser-based conversion electron Mössbauer spectroscopy for a precise energy determination of  $^{229}\text{Th}$ , *Hyperfine Interactions* **240**, 23 (2019).

[24] E. V. Tkalya, C. Schneider, J. Jeet, and E. R. Hudson, Radiative lifetime and energy of the low-energy isomeric level in  $^{229}\text{Th}$ , *Phys. Rev. C* **92**, 054324 (2015).

[25] E. R. Hudson, U.S. Provisional Patent Application No. 63/814,873 (2025).

[26] E. T. Rodine and P. L. Land, Electronic defect structure of single-crystal  $\text{ThO}_2$  by thermoluminescence, *Phys. Rev. B* **4**, 2701 (1971).

[27] B. Seiferle, L. von der Wense, and P. G. Thirolf, Lifetime measurement of the  $^{229}\text{Th}$  nuclear isomer, *Phys. Rev. Lett.* **118**, 042501 (2017).

[28] R. Gillis, *Determining The Extreme Ultraviolet Constant of Thoria by Spectral Ellipsometry*, Bachelor's thesis, Brigham Young University (2007).

[29] M. P. Seah and W. A. Dench, Quantitative electron spectroscopy of surfaces: A standard data base for electron inelastic mean free paths in solids, *Surface and Interface Analysis* **1**, 2 (1979), <https://analyticalsciencejournals.onlinelibrary.wiley.com/doi/pdf/10.1002/sia.740010103>.

[30] S. Stellmer, Y. Shigekawa, V. Rosecker, G. A. Kazakov, Y. Kasamatsu, Y. Yasuda, A. Shinohara, and T. Schumm, Toward an energy measurement of the internal conversion electron in the deexcitation of the  $^{229}\text{Th}$  isomer, *Phys. Rev. C* **98**, 014317 (2018).

[31] J. F. Ziegler, M. D. Ziegler, and J. P. Biersack, SRIM: The stopping and range of ions in matter (2010), *Nucl. Instrum. Methods Phys. Res. B* **268**, 1818 (2010).

[32] J. Jeet, *Search for the low lying transition in the  $^{229}\text{Th}$  Nucleus*, Ph.D. thesis, University of California, Los Angeles (2018).

[33] L. von der Wense, B. Seiferle, M. Laatiaoui, J. B. Neumayr, H.-J. Maier, H.-F. Wirth, C. Mokry, J. Runke, K. Eberhardt, C. E. Düllmann, N. G. Trautmann, and P. G. Thirolf, Direct detection of the  $^{229}\text{Th}$  nuclear clock transition, *Nature* **533**, 47 (2016).

[34] U. C. Perera, H. W. T. Morgan, E. R. Hudson, and A. Derevianko, *Host-dependent frequency offsets in  $^{229}\text{Th}$  nuclear clockwork* (2025), [arXiv:2503.20984 \[physics.atom-ph\]](https://arxiv.org/abs/2503.20984).

[35] J. Callaway, *Quantum Theory of the Solid State*, 2nd ed. (Academic Press, San Diego, CA, 1991).

[36] A. Mock, C. Dugan, S. Knight, R. Korlacki, J. M. Mann, M. M. Kimani, J. C. Petrosky, P. A. Dowben, and M. Schubert, Band-to-band transitions and critical points in the near-infrared to vacuum ultraviolet dielectric functions of single crystal urania and thoria, *Applied Physics Letters* **114**, 10.1063/1.5087059 (2019).

[37] C. Dugan, L. Wang, K. Zhang, J. M. Mann, M. M. Kimani, W.-N. Mei, P. A. Dowben, and J. Petrosky, Interband transitions and critical points of single-crystal thoria compared with urania, *physica status solidi (b)* **259**, 10.1002/pssb.202200238 (2022).

[38] S. Maintz, V. L. Deringer, A. L. Tchougréeff, and R. Dronskowski, Analytic projection from plane-wave and paw wavefunctions and application to chemical-bonding analysis in solids, *Journal of Computational Chemistry* **34**, 2557–2567 (2013).

[39] P. V. Bilous, N. Minkov, and A. Pálffy, Electric quadrupole channel of the 7.8 eV  $\text{Th}$  229 transition, *Phys. Rev. C* **97**, 2 (2018).

[40] L. von der Wense and C. Zhang, Concepts for direct frequency-comb spectroscopy of  $^{229}\text{Th}$  and an internal-conversion-based solid-state nuclear clock, *The European Physical Journal D* **74**, 146 (2020).

[41] J. Belle and R. M. Berman, *Thorium dioxide: properties and nuclear applications*, Tech. Rep. (USDOE Assistant Secretary for Nuclear Energy, Washington, DC. Office of Naval Reactors, 1984).

[42] W. G. Rellergert, D. DeMille, R. R. Greco, M. P. Hehlen, J. R. Torgerson, and E. R. Hudson, Constraining the evolution of the fundamental constants with a solid-state optical frequency reference based on the  $^{229}\text{Th}$  nucleus, *Phys. Rev. Lett.* **104**, 200802 (2010).

[43] J.-F. Lin, J. S. Tse, E. E. Alp, J. Zhao, M. Lerche, W. Sturhahn, Y. Xiao, and P. Chow, Phonon density of states of  $\text{Fe}_2\text{O}_3$  across high-pressure structural and electronic transitions, *Phys. Rev. B* **84**, 064424 (2011).

[44] H. Wang, A. Braun, S. P. Cramer, L. B. Gee, and Y. Yoda, Nuclear resonance vibrational spectroscopy: A modern tool to pinpoint site-specific cooperative processes, *Crystals* **11**, 10.3390/crust11080909 (2021).

[45] S. Banerjee, H. P. Gupta, and S. A. Bhardwaj, Nuclear power from thorium: different options, *Current Science* **111**, 1607 (2016).

[46] L. von der Wense, P. V. Bilous, B. Seiferle, S. Stellmer, J. Weitenberg, P. G. Thirolf, A. Pálffy, and G. Kazakov, The theory of direct laser excitation of nuclear transitions, *The European Physical Journal A* **56**, 176 (2020).

- [47] V. A. Alekseev and D. W. Setser, A pulsed source for Xe(6s[3/2]1) and Xe(6s'[1/2]1) resonance state atoms using two-photon driven amplified spontaneous emission from the Xe(6p) and Xe(6p') states, *The Journal of Chemical Physics* **105**, 4613 (1996), [https://pubs.aip.org/aip/jcp/article-pdf/105/11/4613/19016841/4613\\_1\\_online.pdf](https://pubs.aip.org/aip/jcp/article-pdf/105/11/4613/19016841/4613_1_online.pdf).
- [48] M. B. Rankin, J. P. Davis, C. Giranda, and L. C. Bobb, Two-photon-excited bidirectional emission in xenon, *Optics Communications* **70**, 345 (1989).
- [49] H. A. Bethe, S. S. Schweber, and F. de Hoffmann, *Mesons and Fields, Volume I: Fields* (Row, Peterson and Company, Evanston, IL, 1955).
- [50] D. Koelling and B. Harmon, A technique for relativistic spin-polarised calculations, *Journal of Physics C: Solid State Physics* **10**, 3107 (1977).
- [51] W. R. Johnson, *Atomic structure theory* (Springer, 2007).
- [52] M. S. Safranova, U. I. Safranova, A. G. Radnaev, C. J. Campbell, and A. Kuzmich, Magnetic dipole and electric quadrupole moments of the  $^{229}\text{Th}$  nucleus, *Physical Review A* **88**, 6 (2013).
- [53] C. J. Campbell, A. G. Radnaev, and A. Kuzmich, Wigner crystals of  $^{229}\text{Th}$  for optical excitation of the nuclear isomer, *Phys. Rev. Lett.* **106**, 223001 (2011).
- [54] G. Kresse and J. Furthmuller, Efficient iterative schemes for ab initio total-energy calculations using a plane-wave basis set, *Physical Review B* **54**, 11169 (1996).
- [55] P. E. Blochl, Projector augmented wave method, *Physical Review B* **50**, 17953 (1994).
- [56] J. P. Perdew, K. Burke, and M. Ernzerhof, Generalized gradient approximation made simple, *Physical Review Letters* **77**, 3865 (1996).
- [57] M. Shishkin and G. Kresse, Implementation and performance of the frequency-dependent  $GW$  method within the paw framework, *Physical Review B* **74**, 10.1103/PhysRevB.74.035101 (2006).
- [58] M. Shishkin and G. Kresse, Self-consistent  $GW$  calculations for semiconductors and insulators, *Physical Review B* **75**, 10.1103/PhysRevB.75.235102 (2007).
- [59] P. Liu, M. Kaltak, J. Klimes, and G. Kresse, Cubic scaling  $GW$ : Towards fast quasiparticle calculations, *Physical Review B* **94**, 10.1103/PhysRevB.94.165109 (2016).
- [60] S. Albrecht, L. Reining, R. Del Sole, and G. Onida, Ab initio calculation of excitonic effects in the optical spectra of semiconductors, *Physical Review Letters* **80**, 4510–4513 (1998).
- [61] M. Rohlffing and S. G. Louie, Electron-hole excitations in semiconductors and insulators, *Physical Review Letters* **81**, 2312–2315 (1998).
- [62] F. Tran and P. Blaha, Accurate band gaps of semiconductors and insulators with a semilocal exchange-correlation potential, *Physical Review Letters* **102**, 226401 (2009).
- [63] A. D. Becke and E. R. Johnson, A simple effective potential for exchange, *Journal of Chemical Physics* **124**, 221101 (2006).

## SUPPLEMENTAL INFORMATION

## EXPECTED INTERNAL CONVERSION SIGNAL

The incident VUV flux is attenuated, so that it follows  $\varphi_0 e^{-\alpha z}$  where  $\alpha$  is the VUV attenuation coefficient. The number of excited thorium atoms in a target of length  $L$  should go as [46]

$$N_e \approx \frac{4}{6} \frac{\lambda^2}{2\pi} \frac{n_{\text{Th}}}{\Gamma_L} \frac{T|\tilde{n}|^2}{\text{Re}[\tilde{n}]} \frac{\varphi_0(1 - e^{-\alpha L})}{\alpha} \times \frac{1}{1 + 4 \left( \frac{\delta}{\Gamma_L} \right)^2} \times \left( \frac{t_e}{\tau_{\text{rad}}} \right), \quad (2)$$

where  $\lambda$  is the vacuum transition wavelength,  $n_{\text{Th}}$  is the density of  $^{229}\text{Th}$  in the  $^{229}\text{ThO}_2$  target,  $\Gamma_{\text{rad}} = 1/\tau_{\text{rad}}$  is the vacuum radiative decay rate,  $\Gamma_L$  is the VUV laser bandwidth,  $\Gamma_{\text{IC}} = 1/\tau_{\text{IC}}$  is the IC decay rate,  $\delta$  is the laser detuning,  $\varphi_0$  is incident the laser photon flux,  $L$  is the target thickness,  $T$  is the transmission of the VUV laser into the target, and  $\tilde{n} = n - i\kappa$  is the complex index of refraction with  $\kappa = \lambda\alpha/4\pi$ . The target was produced using a 0.75:0.25  $^{229}\text{Th}:\text{Th}^{232}$  isotope mix from Oak Ridge National Lab, leading to an effective  $^{229}\text{Th}$  density of  $n_{\text{Th}} = 0.75 \times 2.28 \times 10^{22} \text{ cm}^{-3}$  [41].

TABLE I. Parameter values and estimated relative errors used in calculation of expected IC signal. Relative uncertainties labeled by an asterisk (\*) follow log-normal distribution and should be read as  $\ln(X/\bar{X})$ . 0 error entries correspond to assumed values from literature.

Parameter	Value	Rel. Err.
$n_{\text{Th}}$	$1.71 \times 10^{22} \text{ cm}^{-3}$	0 (Ref. [41])
$L$	10 nm	0.7*
$\Gamma_L$	$2\pi \times 12 \text{ GHz}$	0.25
$\alpha$	$0.1 \text{ nm}^{-1}$	0 (Ref. [28])
$n$	2.34	0 (Ref. [28])
$t_i$	$6 \mu\text{s}$	1e-4
$\tau_{\text{rad}}$	1800 s	0.07
$\tau_{\text{IC}}$	$10 \mu\text{s}$	0.1
$T\eta_e$	$1 \times 10^{-4}$	0.7*
$\eta_c$	0.7	0.35*

From the number of excited  $^{229}\text{Th}$  nuclei, the number of detected IC electrons is given by

$$N_{\text{det}} = \eta_e \eta_c N_e \times e^{-t_i/\tau_{\text{IC}}} \quad (3)$$

where  $\eta_e$  is the extraction efficiency from the  $^{229}\text{ThO}_2$  target,  $\eta_c$  is the collection efficiency, and  $t_i$  is the start of the acquisition time window. The extraction efficiency represents the probability that an IC electron is able to leave the  $^{229}\text{ThO}_2$  target, and combines many physical processes such as whether the electron is promoted high enough into the conduction band to overcome the work function barrier, whether the electron inelastically scatters, whether surface conditions are favorable, etc. Due to all of these confounding factors, theoretical calculation of  $\eta_e$  is difficult, and it must be estimated from experiment. To do this, we make the assumption that the probability for a photoelectron promoted by a VUV photon to leave the target is the same as an IC electron promoted by an excited  $^{229}\text{Th}$  nucleus. By making this assumption we are able to use the efficiency with which photoelectrons are generated by our VUV laser system to obtain an estimate of  $T\eta_e$ . The collection efficiency  $\eta_c$  is simply the efficiency with which electrons that leave the target are detected on the MCP given the voltage biasing and magnetic field configuration used in the experiment. This can readily be determined by measuring the ratio of the number of photoelectrons collected on the MCP front plate relative to the number of photoelectrons leaving the target.

Using the values listed in Table I, the expected on-resonance IC signal was estimated to be  $N_{\text{det}}/(\hbar\omega_0\varphi_0 t_e) = 0.15_{-0.09}^{+0.25} e^-/\mu\text{J}/\text{shot}$ .

#### Quenching of ASE in Xe Four-wave Mixing

The four-wave mixing process can produce a beam of amplified spontaneous emission (ASE) along the beam axis, complicating detection. The origin of the ASE is resonant excitation by the 249.6 nm laser of the  $5p^6 \text{ }^1S_0 \rightarrow 5p^5 \left( ^2P_{3/2}^o \right) 6p^2 [1/2]_0$  transition. Any Xe population not participating in the four-wave mixing process will be left in the excited two-photon state. This  $5p^5 \left( ^2P_{3/2}^o \right) 6p^2 [1/2]_0$  (abbreviated as  $6p^2 [1/2]_0$ ) state will then decay to the

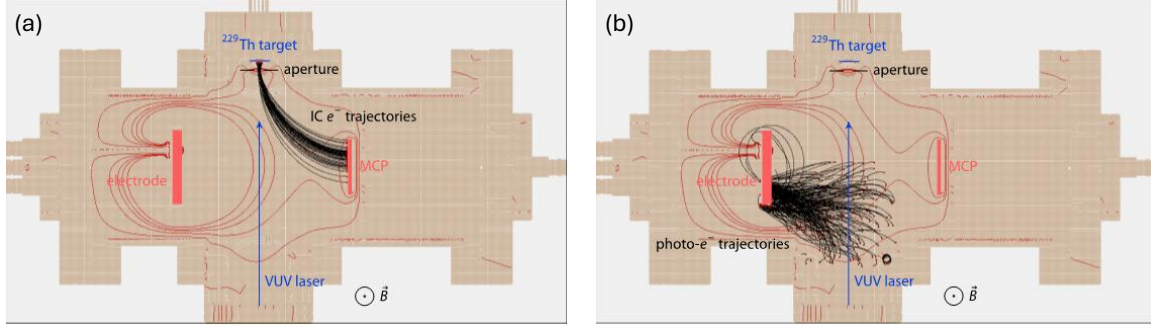


FIG. 4. SIMION simulations of electron trajectories under the voltage biasing and static magnetic field used in the experiment. (a) Trajectories of IC electrons from the target region. The magnetic field bends them towards the detection MCP through a saddle in the electric potential. (b) The trajectories of photoelectrons generated by VUV scattered light at random locations in the chamber. Most either crash into the chamber walls or end up falling into the electrode biased at +2500V.

$5p^5 \left( ^2P_{3/2}^o \right) 6s^2 [3/2]_1^o$  (abbreviated as  $6s^2 [3/2]_1^o$ ) by 828 nm emission in  $\approx 30$  ns, and the  $6s^2 [3/2]_1^o$  state will decay to the  $^1S_0$  ground state by emission of a 147 nm photon in  $\approx 3.7$  ns. If the Xe pressure is in the several hundred Pa range, as it is for efficient four-wave mixing, there are enough nearby Xe atoms that they may re-absorb these 828 nm and 147 nm photons. Effectively, this leads to radiation trapping which extends the effective fluorescence lifetime of the Xe spontaneous emission [47]. At the same time the 828/147 nm spontaneous emission will experience gain as it stimulates Xe in the excited  $6p^2 [1/2]_0$  and  $6s^2 [3/2]_1^o$  to emit, yielding amplified spontaneous emission (ASE). This gain will be highly directional, since the excited Xe will essentially lie in a column defined by the propagation of the 249.6 nm pulse of the pump laser. This interplay between radiation trapping and ASE will then yield bi-directional emission from the Xe cell along the pumping axis, which will have a timescale much longer than the spontaneous emission lifetime of the excited states [48].

To mitigate this effect, we introduce N<sub>2</sub> gas in the Xe, which quenches the excited state Xe population via collision.

#### Simulation of Electron Trajectories

SIMION simulations were carried out in order to determine a combination of voltage biasing and static magnetic field that would guide IC electrons to our detector while diverting background photoelectrons to a secondary electrode. The voltage biasing chosen during the IC observation period was to have the target at -405 V, the front aperture of the target mount at +135V, the front of the detection MCP at +140 V, and the secondary electrode at +2500V. The magnetic field was set to  $\approx 3.5$  G. As can be seen in Fig. 4(a), under the voltage biasing described there is a "saddle" in the potential through which the IC electrons that have been accelerated by our target mount system can be made to travel through by the magnetic field. Meanwhile, as can be seen in Fig. 4(b), electrons that are generated randomly throughout the chamber with  $\sim 8$  eV of kinetic energy either crash into the chamber wall or fall into the sacrificial electrode.

#### PREPARATION OF THE TARGET

The target used in this study was prepared in an electrodeposition buffer solution of NaOH and sulfuric acid. <sup>229</sup>Th material was deposited onto the stainless steel disk until target activity was reached, whereupon a quench was performed with ammonium hydroxide. The disk was then heated overnight at 200-300 °C in ambient atmosphere.

While the electrodeposited target is likely a mixture of Th hydroxides, oxides, and metal impurities, the use of low impurity (>99.99% grade) chemicals during electrodeposition and heat treatment in air lead us to assume it is predominantly Th in an oxidized state. As the most stable oxide form, we assume the target is predominately <sup>229</sup>ThO<sub>2</sub>.

#### INTERNAL CONVERSION RATE DERIVATION

We consider the IC processes in an insulator, when the bandgap  $\Delta$  is smaller than the nuclear isomer energy  $\omega_{\text{nuc}}$ . In the IC process, the nuclear excitation is transferred to the electrons, spawning a particle-hole pair, with a valence

band electron promoted into the conduction band leaving behind a hole in the valence band, see Fig. 5.

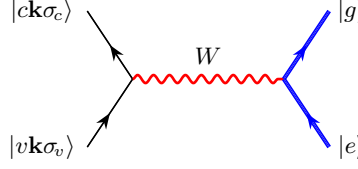


FIG. 5. Feynman diagram of the internal conversion process. Single black strokes represent the electron lines, while the double blue ones denote the nuclear lines. The interaction is mediated by a virtual photon exchange, corresponding to the hyperfine interaction  $W$ . The crystal momentum  $\mathbf{k}$  is conserved in this process.

The  $^{229}\text{Th}$  nuclear subsystem is modeled as two distinct energy levels: the ground state  $|g\rangle$  with nuclear spin  $I_g = 5/2$  and the excited (isomeric) state  $|e\rangle$  with  $I_e = 3/2$ , separated by the energy gap  $\omega_{\text{nuc}}$ .

The IC process is mediated by the hyperfine interaction (HFI). In a crystal, containing  $\mathcal{N}$   $^{229}\text{Th}$  nuclei with one  $^{229}\text{Th}$  per unit cell, HFI reads

$$W(\mathbf{r}) = \sum_{\nu=1}^{\mathcal{N}} \mathcal{M}(\mathbf{R}_\nu) \cdot \mathcal{T}(\mathbf{r} - \mathbf{R}_\nu), \quad (4)$$

where we sum over unit cells,  $\mathcal{M}(\mathbf{R}_\nu)$  is a  $^{229}\text{Th}$  nuclear magnetic moment operator and the  $^{229}\text{Th}$ -centered  $\mathcal{T}$  is a rank-1 tensor acting on the electronic degrees of freedom. The nuclear electric-quadrupolar and higher-rank HFI interactions can be added in a similar fashion. For  $^{229}\text{ThO}_2$ , due to the cubic symmetry, the electric-quadrupole contribution vanishes.

To compute the IC rate, we use the Fermi's golden rule. The initial state of the electron subsystem is a fully-occupied valence band  $|\tilde{0}\rangle$ , and the final state is the particle-hole excitation  $a_{c\mathbf{k}\sigma_c}^\dagger a_{v\mathbf{q}\sigma_v} |\tilde{0}\rangle$  with energy  $\varepsilon_{c\mathbf{k}} - \varepsilon_{v\mathbf{q}}$ , where  $\varepsilon_{c\mathbf{k}}$  and  $\varepsilon_{v\mathbf{q}}$  are the band functions of the conduction (c) and the valence (v) bands. Then, the final state quantum numbers are spanned by crystal momenta  $\mathbf{k}$ ,  $\mathbf{q}$  and two electron spin projections. We also sum over the nuclear ground state magnetic quantum numbers  $M_g$  and average over the nuclear isomer state magnetic quantum numbers  $M_e$ ,

$$\Gamma_{\text{IC}}^{(\mathcal{N})} = \frac{2\pi}{\hbar} \frac{1}{2I_e + 1} \sum_{M_g M_e} \sum_{\sigma_c \sigma_v} \int_{\text{BZ}} d^3 k \int_{\text{BZ}} d^3 q |\langle c\mathbf{k}\sigma_c | W^{ge} | v\mathbf{q}\sigma_v \rangle|^2 \delta(\varepsilon_{c\mathbf{k}} - \varepsilon_{v\mathbf{q}} - \omega_{\text{nuc}}). \quad (5)$$

The integrations are carried over the Brillouin zone (BZ). We use conventions of Ref. [35] in our derivation.

The HFI, Eq. (4) is cell-periodic, and its matrix element  $\langle c\mathbf{k}\sigma_c | W^{ge} | v\mathbf{q}\sigma_v \rangle$  between Bloch functions can be reduced from an integration over the entire crystal to an integration over a single unit cell. The result reads

$$\langle c\mathbf{k}\sigma_c | W^{ge} | v\mathbf{q}\sigma_v \rangle = \delta(\mathbf{k} - \mathbf{q}) W_{c\sigma_c v\sigma_v}^{ge}(\mathbf{k}) \quad (6)$$

with

$$W_{c\sigma_c v\sigma_v}^{ge}(\mathbf{k}) \equiv \frac{(2\pi)^3}{\Omega} \langle g | \mathcal{M} | e \rangle \cdot \int_{\Omega} d^3 r u_{c\mathbf{k}}^*(\mathbf{r}) \chi_{\sigma_c}^\dagger \mathcal{T}(\mathbf{r}) \chi_{\sigma_v} u_{v\mathbf{k}}(\mathbf{r}). \quad (7)$$

Here  $\Omega$  is the unit cell volume,  $u_{\dots}(\mathbf{r})$  are cell-periodic envelopes of Bloch functions [35], and  $\chi$  are the conventional electron spinors. Note that the cell-periodicity imposes conservation of crystal momentum,  $\mathbf{k} = \mathbf{q}$ .

Now with this matrix element, we evaluate the IC rate.

$$\Gamma_{\text{IC}}^{(\mathcal{N})} = \frac{2\pi}{\hbar} \frac{1}{2I_e + 1} \sum_{M_g M_e} \sum_{\sigma_c \sigma_v} \int d^3 k \int d^3 q |W_{c\sigma_c v\sigma_v}^{ge}(\mathbf{k})|^2 \delta(\mathbf{k} - \mathbf{q}) \delta(\mathbf{k} - \mathbf{q}) \delta(\varepsilon_{c\mathbf{k}} - \varepsilon_{v\mathbf{q}} - \omega_{\text{nuc}}) \quad (8)$$

There is a product of two identical delta functions.  $\mathbf{q}$  is replaced by  $\mathbf{k}$  while integrating over  $\mathbf{q}$ , but we encounter  $\delta(\mathbf{0}) = \lim_{\Delta\mathbf{q} \rightarrow 0} \delta(\Delta\mathbf{q})$ . Using the following identity for each component of  $\Delta\mathbf{q}$ :

$$\lim_{\Delta q_x \rightarrow 0} \delta(\Delta q_x) = \lim_{L_x \rightarrow \infty} \lim_{\Delta q_x \rightarrow 0} \frac{1}{2\pi} \int_{-L_x/2}^{L_x/2} e^{i\Delta q_x x} dx = \frac{L_x}{2\pi},$$

where  $L_x$  is the crystal size in the x-direction, we can show that

$$\lim_{\Delta\mathbf{q}\rightarrow 0} \delta(\Delta\mathbf{q}) = \frac{V_{\text{xtal}}}{(2\pi)^3},$$

where the crystal volume  $V_{\text{xtal}} = L_x L_y L_z$ . This is similar to the formal time-domain limit in deriving the Fermi's golden rule, see, e.g., p. 72 of Ref. [49].

Thereby, the IC rate per crystal volume

$$\Gamma_{\text{IC}}^{(\mathcal{N})}/V_{\text{xtal}} = \frac{2\pi}{\hbar} \frac{1}{(2\pi)^3} \frac{1}{2I_e + 1} \sum_{M_g M_e} \sum_{\sigma_c \sigma_v} \int_{\text{BZ}} d^3 k |W_{c\sigma_c v\sigma_v}^{ge}(\mathbf{k})|^2 \delta(\varepsilon_{c\mathbf{k}} - \varepsilon_{v\mathbf{k}} - \hbar\omega_{\text{nuc}}) \quad (9)$$

The assumption made during the derivation was that all  $\mathcal{N}$   $^{229}\text{Th}$  nuclei were initially in the excited (isomer) state. Consider an ensemble of quantum emitters, with  $N(t)$  being the number of emitters in the excited state at time  $t$ . With a single emitter decay rate  $\gamma$  and

$$\begin{aligned} dN/dt &= -\gamma N(t) \Rightarrow N(t) = N(0) \exp\{-\gamma t\} \\ &\Rightarrow \text{Ensemble decay rate } \Gamma = -dN/dt = \gamma N(0) \exp\{-\gamma t\}. \end{aligned} \quad (10)$$

We see that the ensemble decay rate  $\Gamma$  at  $t = 0$  is  $\gamma N(0)$ . The experimentally relevant excited state population, however, decays as  $\exp\{-\gamma t\}$ . Based on this discussion, we define the experimentally measured IC decay rate

$$\Gamma_{\text{IC}} = \Gamma_{\text{IC}}^{(\mathcal{N})}/\mathcal{N} = \Omega \Gamma_{\text{IC}}^{(\mathcal{N})}/V_{\text{xtal}}. \quad (11)$$

Following the derivation of interband electromagnetic absorption rates [35], we define a surface  $S_E$  of constant energy in  $\mathbf{k}$ -space through an implicit relation  $\varepsilon_{c\mathbf{k}} - \varepsilon_{v\mathbf{k}} = \hbar\omega_{\text{nuc}}$ . If the matrix element remains reasonably constant on  $S_E$ , the rate simplifies to

$$\Gamma_{\text{IC}} = \frac{1}{\tau_{\text{IC}}} = \frac{2\pi}{\hbar} \frac{1}{2I_e + 1} \sum_{M_g M_e} \sum_{\sigma_c \sigma_v} \overline{|W_{c\sigma_c v\sigma_v}^{ge}(\mathbf{k})|^2} G_{cv}(\hbar\omega_{\text{nuc}}), \quad (12)$$

with the joint density of states (JDOS)

$$G_{cv}(E) = \frac{\Omega}{(2\pi)^3} \int_{\text{BZ}} d^3 k \delta(\varepsilon_{c\mathbf{k}} - \varepsilon_{v\mathbf{k}} - E) = \frac{\Omega}{(2\pi)^3} \int \frac{dS_E}{|\nabla_{\mathbf{k}}(\varepsilon_{c\mathbf{k}} - \varepsilon_{v\mathbf{k}})_E|}. \quad (13)$$

With this simplification,  $\overline{|W_{c\sigma_c v\sigma_v}^{ge}(\mathbf{k})|^2}$  has the meaning of  $|W_{c\sigma_c v\sigma_v}^{ge}(\mathbf{k})|^2$  averaged over the surface of constant energy  $S_E$ .

This concludes the derivation of the IC rate, Eq.(1) of the main text.

As a side note, notice that the electromagnetic absorption coefficient at laser frequency  $\omega_{\text{nuc}}$  is proportional to the same JDOS  $G_{cv}(\hbar\omega_{\text{nuc}})$ . This can be used to back out the JDOS value from the laser absorption measurements at a frequency slightly detuned away from  $\omega_{\text{nuc}}$ .

To proceed with the computation of the hyperfine matrix element, we expand the functions  $u_{c\mathbf{k}}(\mathbf{r})$  in terms of the Th atomic states. Due to the short-range nature of the hyperfine interaction, relativistic effects play an important role. As a result, we use relativistic Dirac spinors for the Th atomic states. However, Eq. (7) is given in terms of nonrelativistic (or scalar relativistic [50]) two-component spinors. Here, for simplicity, we replace Eq. (7) with

$$W_{c\sigma_c v\sigma_v}^{ge}(\mathbf{k}) \equiv \frac{(2\pi)^3}{\Omega} \langle g | \mathcal{M} | e \rangle \cdot \int_{\Omega} d^3 r u_{c\mathbf{k}\sigma_c}^{\dagger}(\mathbf{r}) \mathcal{T}(\mathbf{r}) u_{v\mathbf{k}\sigma_v}(\mathbf{r}), \quad (14)$$

where  $u_{n\mathbf{k}\sigma_n}(\mathbf{r})$  is now a four-component Dirac spinor with momentum  $\mathbf{k}$  and spin projection  $\sigma_n$ .

The crystal function  $u_{c\mathbf{k}\sigma_c}(\mathbf{r})$  (and similarly  $u_{v\mathbf{k}\sigma_v}(\mathbf{r})$ ) may be expanded in terms of the Th atomic states of definite principle and angular momentum quantum numbers  $\varphi_{nlm}(\mathbf{r})$

$$u_{c\mathbf{k}\sigma_n}(\mathbf{r}) = \sqrt{\frac{\Omega}{(2\pi)^3}} \sum_{nlm} a_{nlm}(\mathbf{c}\mathbf{k}\sigma_n) \varphi_{nlm}(\mathbf{r}) + \dots, \quad (15)$$

where the ellipses denote contributions from O atomic states, which, due to their insignificant overlap with the Th nucleus, do not affect the HFI matrix element. Using the expansion (15), we may write

$$W_{c\sigma_c v\sigma_v}^{ge}(\mathbf{k}) = \sum_{njl} \sum_{n'j'l'm'} a_{njl}^*(c\mathbf{k}\sigma_c) a_{n'j'l'm'}(v\mathbf{k}\sigma_v) \tilde{W}_{njl m n'j'l'm'}^{ge}, \quad (16)$$

where  $\tilde{W}_{njl m n'j'l'm'}^{ge} = \langle g|\mathcal{M}|e\rangle \cdot \int_{\Omega} d^3r \varphi_{njl}^{\dagger}(\mathbf{r}) \mathcal{T}(\mathbf{r}) \varphi_{n'j'l'm'}(\mathbf{r})$ .

Given the crystal functions and the atomic wavefunctions, the expansion coefficients  $a_{njl}(\mathbf{k}\sigma_n)$  may be computed and the total HFI matrix element obtained. Here, we make a simplifying assumption that only a few terms contribute significantly to the sum (16). Furthermore, we shall neglect the contribution cross terms in  $|W_{c\sigma_c v\sigma_v}^{ge}(\mathbf{k})|^2$ . With these simplifications, the IC rate may be written as

$$\begin{aligned} \Gamma_{\text{IC}} \approx & \frac{\pi}{\hbar} \frac{1}{2I_e + 1} \sum_{M_g M_e} \sum_{njl} \sum_{n'j'l'm'} \left| \tilde{W}_{njl m n'j'l'm'}^{ge} \right|^2 \\ & \times \sum_{\sigma_c \sigma_v} \frac{2\Omega}{(2\pi)^3} \int_{\text{BZ}} d^3k |a_{njl}^*(c\mathbf{k}\sigma_c)|^2 |a_{n'j'l'm'}(v\mathbf{k}\sigma_v)|^2 \delta(\varepsilon_{c\mathbf{k}} - \varepsilon_{v\mathbf{k}} - \hbar\omega_{\text{nuc}}). \end{aligned} \quad (17)$$

Let us now consider the matrix element  $W_{c\sigma_c v\sigma_v}^{ge}(\mathbf{k})$  in more details. Using the Wigner-Eckart theorem, we may write

$$\tilde{W}_{njl m n'j'l'm'}^{ge} = \sum_{\nu=-1}^1 (-1)^{\nu + I_g - M_g + j - m} \begin{pmatrix} I_g & 1 & I_e \\ -M_g & \nu & M_e \end{pmatrix} \begin{pmatrix} j & 1 & j' \\ -m & -\nu & m' \end{pmatrix} \langle g||\mathcal{M}||e\rangle \langle njl||\mathcal{T}||n'j'l'\rangle. \quad (18)$$

Here,  $\langle g||\mathcal{M}||e\rangle \approx 0.84\mu_N$  ( $\mu_N$  is the nuclear magneton) is the reduced matrix element of the nuclear magnetic moment operator (see, e.g. Ref. [12]), and  $\langle njl||\mathcal{T}||n'j'l'\rangle$  is the reduced matrix element of the rank-1 electronic HFI tensor. Th off-diagonal HFI matrix elements are at least two orders of magnitude smaller than the diagonal ones, so the most significant contributions to the IC rate come from terms with  $(njl) = (n'j'l')$ . The reduced matrix element  $\langle njl||\mathcal{T}||njl\rangle$  may be related to the ground state HFI constant  $A_{njl}$  via [51]

$$A_{njl} = \frac{\mu_g}{I_g j} \frac{(2j)!}{\sqrt{(2j-1)!(2j+2)!}} \langle njl||\mathcal{T}||njl\rangle, \quad (19)$$

where  $\mu_g = 0.360(7)\mu_N$  is the magnetic moment of the ground nuclear state [52]. With this, the summations over  $M_g$  and  $M_e$  in Eq. (17) may be carried out, giving

$$\sum_{M_g M_e} \left| \tilde{W}_{njl m n'j'l'm'}^{ge} \right|^2 = \frac{1}{3} \left[ \sum_{\nu=-1}^1 \begin{pmatrix} j & 1 & j' \\ -m & \nu & m' \end{pmatrix}^2 \right] \langle g||\mathcal{M}||e\rangle^2 \langle njl||\mathcal{T}||n'j'l'\rangle^2. \quad (20)$$

To proceed, we make a further assumption that the quantity in the second line of Eq. (17) does not depend strongly on the magnetic quantum numbers  $m$  and  $m'$ , i.e.,

$$\begin{aligned} & \sum_{\sigma_c \sigma_v} \frac{2\Omega}{(2\pi)^3} \int_{\text{BZ}} d^3k |a_{njl}^*(c\mathbf{k}\sigma_c)|^2 |a_{n'j'l'm'}(v\mathbf{k}\sigma_v)|^2 \delta(\varepsilon_{c\mathbf{k}} - \varepsilon_{v\mathbf{k}} - \hbar\omega_{\text{nuc}}) \\ & \approx \sum_{\sigma_c \sigma_v} \frac{2\Omega}{(2\pi)^3} \int_{\text{BZ}} d^3k |a_{njl}(c\mathbf{k}\sigma_c)|^2 |a_{n'j'l'}(v\mathbf{k}\sigma_v)|^2 \delta(\varepsilon_{c\mathbf{k}} - \varepsilon_{v\mathbf{k}} - \hbar\omega_{\text{nuc}}), \end{aligned} \quad (21)$$

then the summation over  $m$  and  $m'$  may be carried out analytically, giving finally

$$\begin{aligned} \Gamma_{\text{IC}} \approx & \frac{\pi}{3\hbar} \frac{1}{2I_e + 1} \langle g||\mathcal{M}||e\rangle^2 \sum_{njl} \sum_{n'j'l'} \langle njl||\mathcal{T}||n'j'l'\rangle^2 \\ & \times \sum_{\sigma_c \sigma_v} \left[ \frac{2\Omega}{(2\pi)^3} \int_{\text{BZ}} d^3k |a_{njl}(c\mathbf{k}\sigma_c)|^2 |a_{n'j'l'}(v\mathbf{k}\sigma_v)|^2 \delta(\varepsilon_{c\mathbf{k}} - \varepsilon_{v\mathbf{k}} - \hbar\omega_{\text{nuc}}) \right]. \end{aligned} \quad (22)$$

One recognizes the quantity in the square bracket as the (twice) projected joint density of states (PJ DOS), which counts the number of allowed transitions at energy  $\hbar\omega_{\text{nuc}}$  between the atomic component  $|n'j'l'm'\rangle$  of  $|v\mathbf{k}\sigma_v\rangle$  and

the atomic component  $|njl m\rangle$  of  $|c\mathbf{k}\sigma_c\rangle$ . In Fig. 3(c) in the main text, we present the most relevant PJDOS. These PJDOS were computed using VASP (see the next section) and are used the scalar relativistic approximation of Koelling & Harmon [50]. To obtain the relativistic PJDOS, we adopt the procedure developed in Ref. [12], i.e., for any  $l > 0$ ,  $|a_{nl-1/2l}(c\mathbf{k}\sigma_c)|^2 = |a_{nl+1/2l}(c\mathbf{k}\sigma_c)|^2 = |a_{nl}|^2/2$  where  $|a_{nl}|^2$  is the VASP projection. As a result, for  $l > 0$  the relativistic  $(njl) \rightarrow (njl)$  PJDOS is a quarter of the scalar relativistic value. On the other hand, since the VASP calculation was spin-independent, the double summation over  $\sigma_c$  and  $\sigma_v$  in Eq. (22) results in a factor of  $2 \times 2 = 4$ . In Table II, we list the HFI constants  $A$ , the corresponding “diagonal” values of the PJDOS at the nuclear energy for various Th atomic states, and the contributions to the IC rate. Using these values, we arrive at an estimate for the IC rate of

$$\Gamma_{\text{IC}} \approx 1.3 \times 10^4 \text{ s}^{-1}, \quad (23)$$

corresponding to an IC lifetime of 80  $\mu\text{s}$ .

TABLE II. Magnetic-dipole  $A$  HFI constants for low-lying levels of  $^{229}\text{Th}^{3+}$ , the corresponding values of PJDOS at the nuclear energy  $\approx 8.35$  eV, and the contributions to the IC rate. The  $A$  constants for  $7s$  and  $6p$  states are computed using our relativistic atomic-structure code with random-phase-approximation (RPA) and perturbative Brueckner-orbital (BO) corrections. The  $A$  constants for  $6d$  and  $5f$  states are taken from experiment [53].

	$A$ (MHz)	PJDOS( $\hbar\omega_{\text{nuc}}$ ) (1/eV)	Contribution to $\Gamma_{\text{IC}}$ ( $\text{s}^{-1}$ )
$7s_{1/2} - 7s_{1/2}$	+6249	$5 \times 10^{-5}$	431
$6p_{1/2} - 6p_{1/2}$	+8604	$2.5 \times 10^{-4}$	8182
$6p_{3/2} - 6p_{3/2}$	+426	$2.5 \times 10^{-4}$	200
$6d_{3/2} - 6d_{3/2}$	+155.3	$2.5 \times 10^{-3}$	267
$6d_{5/2} - 6d_{5/2}$	-12.6	$2.5 \times 10^{-3}$	6.14
$5f_{5/2} - 5f_{5/2}$	+82.0	$2.5 \times 10^{-2}$	2601
$5f_{7/2} - 5f_{7/2}$	+31.4	$2.5 \times 10^{-2}$	915

## COMPUTATIONAL METHODS FOR ELECTRONIC STRUCTURE THEORY

Calculations were performed with VASP [54], version 6.4.2, using the PAW [55] method. The structure of  $\text{ThO}_2$  was optimized with DFT in the conventional unit cell using the PBE [56] functional, 6-6-6  $\Gamma$ -centred  $k$ -mesh and a 500 eV plane wave cutoff. Subsequent electronic structure calculations used the optimized structure in the primitive cell representation.

Parameters for  $G_0W_0$  calculations [57–59], specifically the  $k$ -mesh, plane wave cut-off energy, and the number of frequency grid points (NOMEGA tag in VASP), were tested for convergence of the band gap. The number of unoccupied bands was 812 (there are 12 occupied bands). Results of these tests are shown in Tables III, IV, and V. On the basis of these results, further  $G_0W_0$  calculations were done with an 8-8-8  $k$ -mesh, a 400 eV plane wave cut-off, and 80 frequency grid points.

TABLE III. Convergence of the  $G_0W_0$  band gap with respect to  $k$ -mesh.

mesh	spacing ( $\text{\AA}^{-1}$ )	band gap (eV)
6-6-6	0.05	6.31
7-7-7	0.045	6.21
8-8-8	0.04	6.18
9-9-9	0.035	6.22

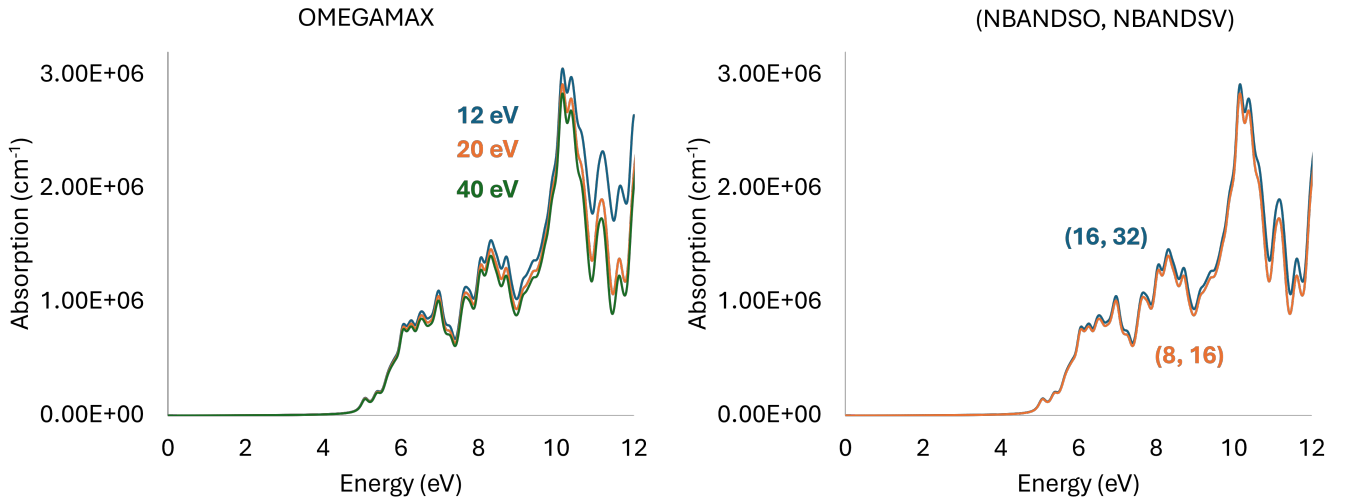
TABLE IV. Convergence of the  $G_0W_0$  band gap with respect to plane wave cut-off.

Cut-off (eV)	band gap (eV)
400	6.31
500	6.30
600	6.29

TABLE V. Convergence of the  $G_0W_0$  band gap with respect to frequency grid points (NOMEGA).

NOMEGA band gap (eV)	
8	7.45
20	6.36
40	6.21
80	6.18

The Bethe-Salpeter equation (BSE) is a two-particle Green's-function formalism to explicitly account for electron–hole interactions in electronic excited states [60, 61]. The  $G_0W_0$ +BSE parameters were converged with respect to the predicted absorption spectrum. The tested parameters were the highest excitation energy (OMEGAMAX) and the number of occupied and unoccupied bands (NBANDSO and NBANDSV) considered in the BSE calculation. Absorption spectra computed with various settings for these methods are shown in Fig. 6. On the basis of these tests, further  $G_0W_0$ +BSE calculations were done with OMEGAMAX = 20 eV and (NBANDSO, NBANDSV) = (8, 16).

FIG. 6. Absorption spectra of  $\text{ThO}_2$  computed with  $G_0W_0$ +BSE using different OMEGAMAX and (NBANDSO, NBANDSV) settings. The meanings of these parameters are given in the text.

We can validate our method against published experimental data by computing the dielectric function with  $G_0W_0$ +BSE. Our computed data, shown in Fig. 7, are an excellent match to the spectroscopic data in Ref. [36].

We also compute the absorption spectrum of  $\text{ThO}_2$  with  $G_0W_0$ +BSE, as shown in Fig. 8. The value at the nuclear transition energy is  $1 \times 10^6 \text{ cm}^{-1} \equiv 0.1 \text{ nm}^{-1}$ , in agreement with ellipsometric measurements [28].

The absorption spectrum plotted in the main text was computed using a 500 eV plane-wave cut-off and the O\_GW pseudopotential, though later testing revealed that these changes did not have a noticeable effect on the calculated absorption spectrum. Absorption spectra and dielectric functions were processed from VASP output with VASPKIT.

## ISOMER SHIFT

The isomer shift originates from differences in the nuclear charge distribution between the ground and excited nuclear states. The value of the shift depends on the local electronic environment of  $^{229}\text{Th}$ . Here we follow the formalism [34] that combines relativistic many-body atomic structure methods with periodic DFT to evaluate the isomer shifts in  $^{229}\text{ThO}_2$ . The scalar relativistic periodic DFT reproduces valence-band properties while relativistic atomic-structure methods captures the essential core-electron relaxation effects. The valence-band (VB) contribution to the isomer shift in  $^{229}\text{Th}$  solid-state hosts is expressed as [34]

$$\delta E_{\text{iso}}^{\text{VB}} = \sum_{\ell} \text{IPDOS}_{\ell} \delta \varepsilon_{\ell}^{\text{iso}}(\text{Th}^{3+}), \quad (24)$$

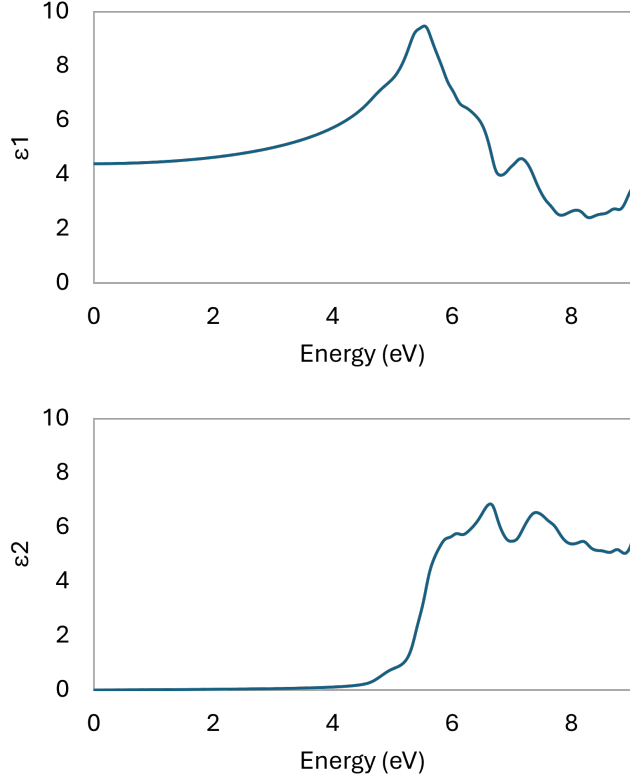


FIG. 7. Real ( $\epsilon_1$ ) and imaginary ( $\epsilon_2$ ) parts of the frequency-dependent dielectric function for bulk  $\text{ThO}_2$  computed with  $G_0W_0+\text{BSE}$ .

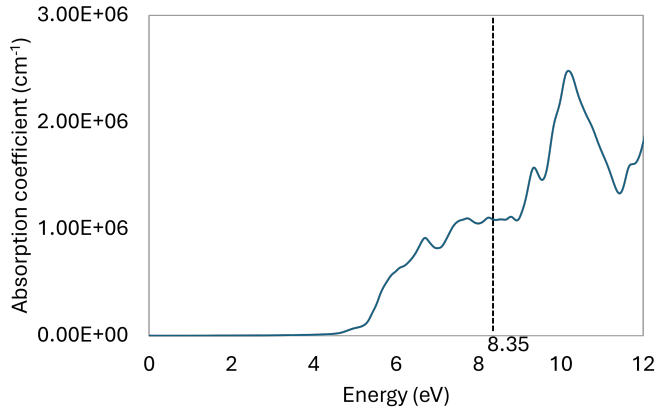


FIG. 8. Absorption spectrum of bulk  $\text{ThO}_2$  computed with  $G_0W_0+\text{BSE}$

where  $\text{IPDOS}_\ell$  denotes the integrated projected (on  $^{229}\text{Th}$ ) valence band density of states for angular-momentum  $\ell$ , and  $\delta\varepsilon_\ell^{\text{iso}}(\text{Th}^{3+})$  are the isomer-shift for the lowest-energy valence orbitals of  $\text{Th}^{3+}$  of angular-momentum  $\ell$ . The VB isomer shift is to be added to the isomer shift in  $^{229}\text{Th}^{4+}$  ion; this contribution remains constant across a wide range of materials. Table VI presents the calculated isomer shifts for  $^{229}\text{ThO}_2$  for three different methods. Compared to the PBE and MBJ [62, 63] methods, the  $G_0W_0$  method includes self-energy correction and, as discussed earlier, we consider it of a higher quality.

Table VII presents the calculated isomer shifts  $\delta E_{\text{iso}}^{\text{VB}}$ , the corresponding nuclear-clock frequencies  $\nu$  of  $^{229}\text{Th}$ , and their offsets  $\Delta\nu$  relative to the  $\text{ThO}_2$  reference for a range of solid-state hosts.

TABLE VI. Integrated partial densities of states,  $\text{IPDOS}_\ell$ , and the products,  $\delta E_{\text{iso},\ell}^{\text{VB}} = \text{IPDOS}_\ell \delta \varepsilon_\ell^{\text{iso}}(\text{Th}^{3+})$  obtained with the three electronic-structure methods. The isomer shift of the solid-state Th clock,  $\delta E_{\text{iso}}^{\text{VB}}$  (bottom row), is the summation over the orbital,  $\ell$  defined in Eq. (24).

$\ell$	$\text{IPDOS}_\ell$	$G_0 W_0$	$\delta E_{\text{iso},\ell}^{\text{VB}}$ (a.u.)	$\text{IPDOS}_\ell$	MBJ	$\delta E_{\text{iso},\ell}^{\text{VB}}$ (a.u.)
<i>s</i>	0.119		$+1.62 \times 10^{-8}$	0.078		$+1.07 \times 10^{-8}$
<i>p</i>	0.435		$-1.69 \times 10^{-9}$	0.408		$-1.58 \times 10^{-9}$
<i>d</i>	0.759		$-2.42 \times 10^{-8}$	0.688		$-2.19 \times 10^{-8}$
<i>f</i>	0.534		$-4.25 \times 10^{-8}$	0.432		$-3.43 \times 10^{-8}$
$\delta E_{\text{iso}}^{\text{VB}}$ (MHz)		-343				-310

TABLE VII. Nuclear-clock frequencies  $\nu$  obtained from the isomer shifts  $\delta E_{\text{iso}}^{\text{VB}}$  and their offsets  $\Delta\nu$  relative to  $\text{ThO}_2$  computed with MBJ. The absolute frequencies are referenced to the free-ion value  $\nu(\text{Th}^{4+}) = 2020\,407\,648(70)$  MHz taken from Ref. [34].

Host	$\delta E_{\text{iso}}^{\text{VB}}$ (MHz)	$\nu$ (MHz)	$\Delta\nu$ (MHz)
$\text{ThO}_2$	-310	2020 407 338(70)	0
$\text{CaF}_2$ F-90°-F, Ref. [34]	-264	2020 407 384(70)	+46
$\text{LiSrAlF}_6$ , Ref. [34]	-234	2020 407 414(70)	+76